

Engineered antibody fragments for immuno-PET imaging of endogenous CD8⁺ T cells in vivo

Richard Tavaré^a, Melissa N. McCracken^b, Kirstin A. Zettlitz^a, Scott M. Knowles^a, Felix B. Salazar^a, Tove Olafsen^a, Owen N. Witte^{b,c,d,e}, and Anna M. Wu^{a,1}

^aCrump Institute for Molecular Imaging and ^bDepartment of Molecular and Medical Pharmacology, David Geffen School of Medicine, ^cHoward Hughes Medical Institute, ^dDepartment of Microbiology, Immunology, and Molecular Genetics, and ^eEli and Edythe Broad Center of Regenerative Medicine and Stem Cell Research, University of California, Los Angeles, CA 90095

Edited* by Michael E. Phelps, University of California, Los Angeles, CA, and approved November 27, 2013 (received for review September 25, 2013)

The noninvasive detection and quantification of CD8⁺ T cells in vivo are important for both the detection and staging of CD8⁺ lymphomas and for the monitoring of successful cancer immunotherapies, such as adoptive cell transfer and antibody-based immunotherapeutics. Here, antibody fragments are constructed to target murine CD8 to obtain rapid, high-contrast immuno-positron emission tomography (immuno-PET) images for the detection of CD8 expression in vivo. The variable regions of two anti-murine CD8-depleting antibodies (clones 2.43 and YTS169.4.2.1) were sequenced and reformatted into minibody (Mb) fragments (scFv-C₃). After production and purification, the Mbs retained their antigen specificity and bound primary CD8⁺ T cells from the thymus, spleen, lymph nodes, and peripheral blood. Importantly, engineering of the parental antibodies into Mbs abolished the ability to deplete CD8⁺ T cells in vivo. The Mbs were subsequently conjugated to S-2-(4-isothiocyanatobenzyl)-1,4,7-triazacyclononane-1,4,7-triacetic acid for ⁶⁴Cu radiolabeling. The radiotracers were injected i.v. into antigen-positive, antigen-negative, immunodeficient, antigen-blocked, and antigen-depleted mice to evaluate specificity of uptake in lymphoid tissues by immuno-PET imaging and ex vivo biodistribution. Both ⁶⁴Cu-radiolabeled Mbs produced high-contrast immuno-PET images 4 h postinjection and showed specific uptake in the spleen and lymph nodes of antigen-positive mice.

The rapid increase of therapeutic antibodies approved by the US Food and Drug Administration (FDA) and those currently in phase I–III clinical trials for oncological, autoimmune, and inflammatory diseases, among other conditions, has benefited from advances in antibody engineering, protein conjugation chemistry, and biomarker identification (1–3). Concurrently, immuno-PET imaging agents based on intact antibodies have shown promise both preclinically and clinically for the detection of cancer in vivo (4). Noninvasive detection of specific biomarkers of disease can provide crucial information for diagnosis, prognosis, response to therapy, dosage for radioimmunotherapy, and targeted therapy selection.

Although much progress has been made in the immuno-PET detection of oncological markers (4), the noninvasive monitoring of immune cells in the fields of oncology, autoimmunity, and infection remains challenging. Practiced methods for lymphocyte detection include isolation of cells from the peripheral blood or, less commonly, the tissue of interest. However, the invasive tissue sampling methods are prone to error and do not provide dynamic information that reflects the number, location, and movement of lymphoid cells. Therefore, problems still exist for the evaluation of immunotherapy protocols due to the lack of effective methods to monitor the extent and duration of the therapy.

Current methods to monitor immune cells noninvasively using emission tomography include direct cell labeling, reporter genes, small-molecule PET tracers, and radiolabeled intact antibodies. The ex vivo direct labeling of immune cells with PET or single-photon emission computed tomography probes before subsequent reinjection and imaging has enabled in vivo trafficking of lymphocytes (5, 6). However, this method has inherent limitations,

such as radioisotope $t_{1/2}$ and cell division in vivo that lead to probe dilution. Reporter gene imaging, whereby cells are transfected with a PET reporter gene that encodes a protein specifically targeted via a radiolabeled reporter probe (7, 8), has been used to image adoptive cell transfer of transduced T-cell receptor-engineered lymphocytes (9). Reporter gene imaging allows for longitudinal tracking of cells but relies on the ex vivo transfection of cells and, for clinical translation, the development of nonimmunogenic PET reporter proteins (8).

In another approach, small-molecule PET probes targeting metabolic pathways, including [¹⁸F]-fluorodeoxyglucose ([¹⁸F]FDG), [¹⁸F]-fluorothymidine ([¹⁸F]FLT), and [¹⁸F]-1-(2-deoxy-2-fluoro-arabinofuranosyl)-cytosine ([¹⁸F]FAC), all have the potential to monitor diverse cell types of both innate and adaptive immunity noninvasively (reviewed in ref. 10). Clinically, [¹⁸F]FDG-PET has been used to evaluate inflammation in a range of diseases. However, in the context of immune cell detection in oncology, false-positive signals can arise from the utilization of glycolysis in both cancerous and immune cells, both innate and adaptive, in the tumor itself or in the draining lymph nodes (11, 12). [¹⁸F]FLT-PET accumulates in highly proliferative tissues, and most research has been focused on cancer detection. [¹⁸F]FLT-PET suffers from high uptake in proliferating bone marrow, therefore limiting detection of lesions in bone. However, [¹⁸F]FLT-PET was used clinically to detect cytotoxic T-lymphocyte antigen-4 blockade-induced cell replication in the spleens of patients with melanoma (13) and, more recently, to detect antigen-specific immune responses in patients with melanoma who have lymph node metastases using dendritic cell therapy (14). [¹⁸F]FAC-PET can distinguish between innate and adaptive immune cells due to the up-regulation of deoxycytidine kinase in proliferating T cells, but the uptake in a Moloney murine sarcoma virus/murine leukemia virus complex-induced sarcoma model was limited to proliferating T cells in the draining lymph nodes and spleen (15). Therefore, like the other metabolic tracers FDG and FLT, FAC uptake due to activation-induced T-cell

Significance

Anti-CD8 immuno-PET imaging agents provide the potential to monitor the localization, migration, and expansion of CD8-expressing cells noninvasively in vivo. Shown here is the successful generation of functional anti-CD8 imaging agents based on engineered antibodies for use in a variety of preclinical disease and immunotherapeutic models.

Author contributions: R.T., T.O., O.N.W., and A.M.W. designed research; R.T., M.N.M., K.A.Z., S.M.K., F.B.S., and T.O. performed research; R.T., M.N.M., K.A.Z., O.N.W., and A.M.W. analyzed data; and R.T. and A.M.W. wrote the paper.

Conflict of interest statement: A.M.W. and T.O. have a financial interest in ImaginAb, Inc. T.O. is an employee of ImaginAb, Inc.

*This Direct Submission article had a prearranged editor.

¹To whom correspondence should be addressed. E-mail: awu@mednet.ucla.edu.

This article contains supporting information online at www.pnas.org/lookup/suppl/doi:10.1073/pnas.1316922111/-DCSupplemental.

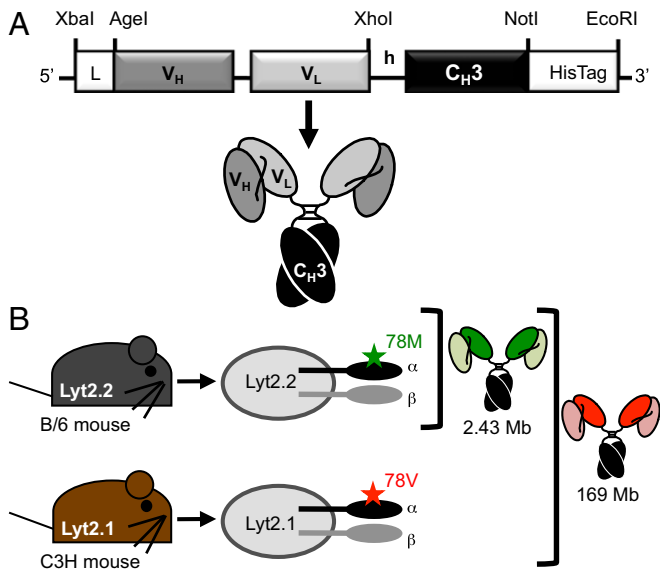


Fig. 1. Mb construction and epitope specificity are shown. (A) Anti-CD8 2.43 and YTS169 Mbs contain the rat V_H-V_L separated by an 18-aa linker, followed by the murine IgG2a hinge (h), murine C_H3, and a C-terminal hexahistidine (HisTag). (B) Murine CD8 α (Lyt2) is expressed as two isoforms, Lyt2.1 and Lyt2.2, that differ in a single amino acid, and it is restricted to specific mouse strains. The 2.43 Mb binds CD8 α only in Lyt2.2⁺ mouse strains, whereas the YTS169 Mb binds CD8 α in all mouse strains.

proliferation is restricted to the draining lymph nodes and was unable to image tumor T-cell infiltration (15). This makes immuno-PET imaging using antibody fragments targeting specific immune cell antigens (i.e., CD8 expressed on cytotoxic T cells and CD4 expressed on helper T cells) potentially critical for immunotherapeutic diagnosis, because the expression of CD8 is present on all cytotoxic T cells and binding is not proliferation-dependent.

Intact antibodies have relatively long serum $t_{1/2}$ s (1–3 wk) compared with their engineered counterparts, such as the diabody and minibody (Mb), which have terminal $t_{1/2}$ s that range from 2 to 5 h and from 5 to 12 h, respectively (16). Although decreasing the total uptake in tumors, the rapid clearance of engineered antibody fragments allows for higher tumor-to-background images at earlier times postinjection (p.i.). This not only allows for the potential of same-day imaging but reduces the overall radiation dose. Furthermore, engineered diabody and Mb fragments are biologically inert because they lack Fc effector functions. Intact antibodies have been used previously to image T cells in patients with a range of disorders (reviewed in ref. 17). The majority of these studies use planar gamma imaging using therapeutic intact mouse anti-human antibodies. The expanding knowledge of the importance of immune cell subtypes in diseases and the improvements in antibody-based immuno-PET imaging indicate that antibody-based imaging of immune cells in vivo should be revisited.

In this report, we develop two anti-murine CD8 Mbs (Fig. 1A) for the detection of CD8 expression. Murine CD8 is a cell surface glycoprotein expressed mainly on a subset of T cells known as cytotoxic T cells and a subset of dendritic cells. Functional CD8 is expressed as either the homodimer CD8 $\alpha\alpha$ or the heterodimer CD8 $\alpha\beta$ of the two isoforms of CD8, α and β . Mice have two alleles for CD8 α , Lyt2.1 and Lyt2.2, which are restricted to certain mouse strains. Lyt2.1, for example, is expressed in the mouse strains CBA, AKR, C3H, and DBA, whereas Lyt2.2 is expressed in the mouse strains BALB/c and C57BL/6 (B/6). The difference between Lyt2.1 and Lyt2.2 is a methionine (Lyt2.2)-to-valine (Lyt2.1) substitution at residue 78 of the mature CD8 α (Fig. 1B).

In this study, the parental antibodies from the hybridomas YTS 169.4.2.1 (YTS169) and 2.43 were engineered into Mb fragments (Fig. 1A). Both the YTS169 and 2.43 antibodies bind mCD8 α (Lyt2). However, they differ in that the YTS169 antibody binds both Lyt2.1 and Lyt2.2, whereas the 2.43 antibody binds an epitope that is Lyt2.2-specific (Fig. 1B). These newly engineered Mbs retained their antigen specificity, as shown by flow cytometry and ⁶⁴Cu immuno-PET imaging. Most importantly, both the 2.43 and YTS169 Mbs produce high-contrast immuno-PET images of CD8⁺ lymphoid organs at only 4 h p.i. This report details successful antibody fragment-based immuno-PET detection of CD8 expression in vivo.

Results

Sequencing Variable Regions of Parental Rat Anti-murine CD8 Antibodies. RT-PCR was repeated until at least two individual experiments produced three replicates of the same sequence for the V_H and V_L domains for each hybridoma for sequence assurance. For further sequence validation of hybridoma 2.43, the V_H and V_L from RT-PCR sequences were confirmed with tryptic digest mass spectrometry (MS) of the parental antibody. V_H amino acid coverage was 35% (41 of 117), including the complete complementarity-determining region 1 (CDR1) and half of CDR2, and V_L amino acid coverage was 62% (66 of 107), including both CDR2 and CDR3. For YTS169, no MS sequence verification was performed.

Production and Characterization of Mb Fragments. Mb purification from NS0 supernatant was performed using nickel-nitrilotriacetic acid (Ni-NTA) columns and imidazole elution (Fig. S1A). SDS/PAGE showed that the Mb eluted between 25 and 45 min (Fig. S1B). The yields of the 2.43 and YTS169 Mbs were 6.6 and 8.9 mg/L, respectively. Purified protein was then analyzed on Superdex 200 size exclusion chromatography (SEC) and compared with reference standards to confirm assembly, purity, and dimerization (Fig. S1C). The 2.43 and YTS169 Mbs are purified as 81% or 23% 80-kDa dimers, respectively, as calculated by peak areas, with the remaining 19% and 77% eluting as higher molecular-weight multimers.

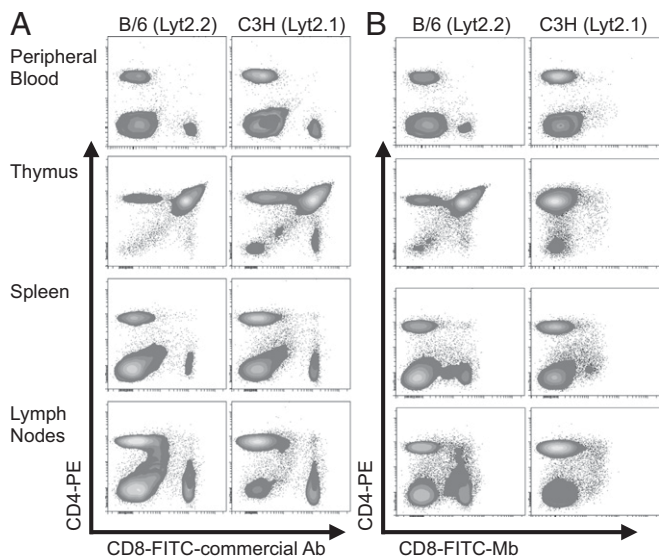


Fig. 2. The 2.43 Mb retains Lyt2.2 antigen specificity. Primary cells isolated from the peripheral blood, thymus, spleen, and lymph nodes of B/6 and C3H mice were stained with phycoerythrin (PE)-anti-CD4 and either a commercial FITC-anti-CD8 antibody (A) or the Lyt2.2-specific FITC-2.43 Mb (B). The lack of CD8-FITC staining in Lyt2.1⁺ C3H mice shows the 2.43-Mb specificity for Lyt2.2⁺ B/6 mice.

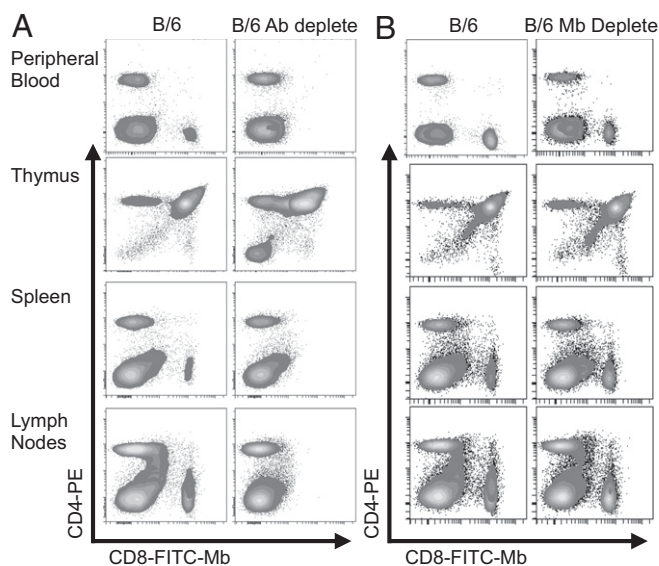


Fig. 3. Anti-CD8 Mb does not deplete CD8-expressing cells in vivo. B/6 mice were treated for three consecutive days with either 330 μ g of anti-CD8 depleting antibody (clone 53-6.7) injected i.p. (A) or 250 μ g of 2.43 Mb injected i.v. (B). Cells were then isolated from the peripheral blood, thymus, spleen, and lymph nodes for staining with anti-CD4-PE and FITC-conjugated 2.43 Mb.

Flow cytometry confirmed epitope specificity of the Mb fragments. The murine CD8⁺ T-cell lymphoma lines BW58 (Lyt2.2⁺) and TK-1 (Lyt2.1⁺) were stained with either 2.43 or YTS169 Mb, followed by anti-mouse IgG2a-phycoerythrin (Fig. S1D). To demonstrate further the epitope specificity of the 2.43-Mb construct, the 2.43 Mb was conjugated to FITC at a 1.4:1 ratio of fluorescein/Mb. Single-cell suspensions from the peripheral blood, thymus, spleen, and lymph nodes of B/6 (Lyt2.2⁺) or C3H (Lyt2.1⁺) mice were stained with either the FITC-2.43 Mb or a commercial FITC-anti-CD8 antibody and anti-CD4 (Fig. 2). The 2.43 Mb shows comparable binding to cells isolated from antigen-positive Lyt2.2 B/6 mice and does not bind CD8 in primary cells from various organs of the antigen-negative Lyt2.1 C3H mice.

To determine the affinity of both the 2.43 and YTS169 Mb, a recombinant soluble CD8 $\alpha\beta$ (sCD8 $\alpha\beta$) heterodimer fusion protein was constructed by removing the transmembrane domains of both CD8 α and CD8 β and fusing them with a 29-aa α -helical linker. The soluble antigen was purified using Ni-NTA affinity chromatography, followed by SEC (Fig. S2). Solution-phase binding of the 2.43 and YTS169 Mbs to the purified sCD8 $\alpha\beta$

antigen was first confirmed by SEC. Briefly, equimolar amounts of soluble antigen and the Mb in question were incubated for 5 min in PBS before SEC analysis. All Mb peaks eluted 2.8–3 min earlier in the presence of sCD8 $\alpha\beta$, confirming Mb and antigen-bound complexes of a larger size. Additionally, the Mb multimer detected by size exclusion eluted 2.5–2.8 min earlier (Fig. S3).

Surface plasmon resonance kinetic analysis was performed using Biacore 3000 (Precision Antibody, Inc.) with immobilized Mb and soluble monomeric sCD8 $\alpha\beta$. The equilibrium constants (K_{dS}) for 2.43 and YTS169 were 34 and 33 nM, respectively. A full analysis is provided in Fig. S4.

In Vivo Depletion. Single-cell suspensions from the spleen, peripheral blood, thymus, and lymph nodes of WT B/6 mice, B/6 mice treated with a CD8-depleting antibody, or B/6 mice treated with the 2.43 Mb were analyzed by flow cytometry for effective CD8 depletion (Fig. 3). Mice treated with the depleting antibody showed >95% loss of CD8⁺ leukocytes, whereas mice treated with the 2.43 Mb did not show a reduction in CD8⁺ leukocytes.

NOTA Conjugation and Radiolabeling. Following conjugation of both 2.43 and YTS169 Mb to S-2-(4-Isothiocyanatobenzyl)-1,4,7-triazacyclononane-1,4,7-triacetic acid (p-SCN-Bn-NOTA) and ⁶⁴Cu radiolabeling, ⁶⁴Cu incorporation was consistently >80% and the radiochemical purity was >98% after spin column purification ($n = 10$ radiolabelings). The immunoreactive fraction of the ⁶⁴Cu-NOTA Mbs ranged from 65 to 75%. The specific activity was between 295 and 370 MBq/mg (8–10 mCi/mg), and mice were injected with 2.6–2.9 MBq (70–80 μ Ci) i.v.

Immuno-PET and ex Vivo Biodistribution. Due to the specificity for Lyt2.2, WT B/6 (Lyt2.2⁺) mice were initially imaged with ⁶⁴Cu-NOTA-2.43 Mb (Fig. 4). High-contrast immuno-PET images showed a high percent-injected dose per gram of tissue (%ID/g) uptake in the spleen, lymph nodes, and liver of the antigen-positive B/6 mice, and ex vivo biodistribution confirmed uptake of $75 \pm 8.5\%$ ID/g, $27 \pm 7.9\%$ ID/g, and $57 \pm 11\%$ ID/g, respectively (Table 1). When injected into antigen-negative Lyt2.1 C3H mice, the ⁶⁴Cu-NOTA-2.43 Mb showed similar %ID/g uptake in the liver and five- to ninefold reduced uptake in the spleen ($15 \pm 2.3\%$ ID/g) and lymph nodes ($2.7 \pm 0.71\%$ ID/g) compared with the B/6 mice (Fig. 5A and Table 1). The average %ID/g blood after only 4 h in B/6 and C3H mice was $0.90 \pm 0.14\%$ ID/g and $1.3 \pm 0.10\%$ ID/g, respectively.

To confirm the radiotracer uptake of ⁶⁴Cu-NOTA-2.43 Mb in antigen-negative C3H mice, the ⁶⁴Cu-NOTA-2.43 Mb was injected into immunodeficient NOD.Cg-Prkdc^{scid} Il2rg^{tm1Wjl}/SzJ (NSG) mice that lack mature T cells, B cells, and natural killer cells. Immuno-PET images and ex vivo biodistribution in NSG mice were very similar to those of the ⁶⁴Cu-NOTA-2.43 Mb in

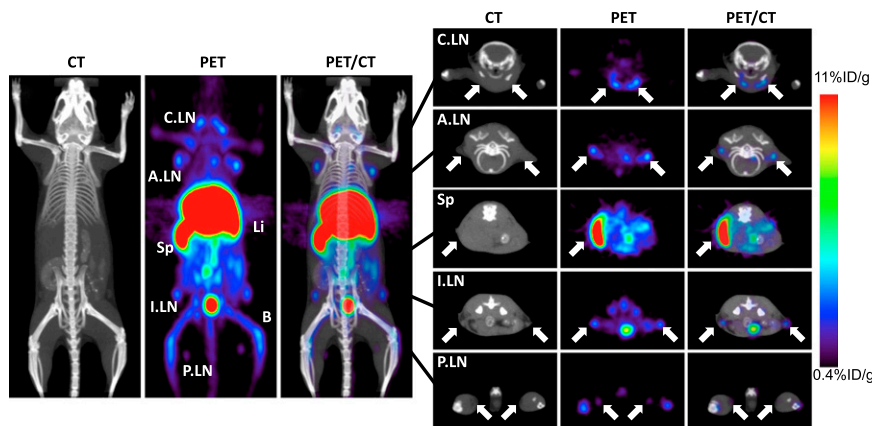


Fig. 4. Immuno-PET imaging of ⁶⁴Cu-NOTA-2.43 Mb 4 h p.i. is shown. Immuno-PET/CT images were acquired 4 h after i.v. injection in B/6 mice. The white arrows (2-mm transverse MIPs) are used to highlight uptake in various lymph nodes (Right) and the spleen seen in the whole-body 20-mm coronal MIPs (Left). A.LN, axillary lymph nodes; B, bone; C.LN, cervical lymph nodes; I.LN, inguinal lymph nodes; Li, liver; MIPs, maximum intensity projections; P.LN, popliteal lymph nodes; Sp, Spleen.

Table 1. Ex vivo biodistribution analysis of ^{64}Cu -NOTA-2.43 Mb 4 h p.i. in Lyt2.2^+ B/6 mice, Lyt2.1^+ C3H mice, NSG SCID mice, antigen-blocked B/6 mice, and antigen-depleted B/6 mice

Organ	%ID/g				
	WT B/6 (n = 6)	WT C3H (n = 3)	NSG (n = 3)	B/6 + block (n = 3)	B/6 + depletion (n = 3)
Blood	0.90 ± 0.14	1.3 ± 0.10**	0.89 ± 0.13	2.1 ± 0.31***	1.9 ± 0.10***
Axillary lymph nodes	27 ± 7.9	2.7 ± 0.71**	N/A	5.0 ± 1.3**	4.5 ± 2.7**
Spleen	75 ± 8.5	15 ± 2.3***	13 ± 3.9***	18 ± 1.9***	15 ± 1.0***
Stomach	1.1 ± 0.42	1.1 ± 0.11	0.43 ± 0.11*	1.0 ± 0.09	1.6 ± 0.92
Intestines	3.8 ± 0.58	3.2 ± 0.17	1.1 ± 0.04***	4.3 ± 0.47	3.4 ± 0.73
Liver	57 ± 11	47 ± 1.6	38 ± 1.0*	71 ± 1.2	59 ± 6.5
Kidneys	5.6 ± 0.72	5.8 ± 0.72	3.8 ± 0.26**	7.0 ± 0.31*	6.4 ± 0.50
Thymus	0.89 ± 0.63	0.46 ± 0.05	2.2 ± 0.89*	1.8 ± 0.42	1.1 ± 0.46
Heart	1.6 ± 0.22	2.3 ± 0.09**	1.3 ± 0.15	3.1 ± 0.36***	2.7 ± 0.19***
Lungs	3.3 ± 1.3	2.3 ± 0.61	1.2 ± 0.11	3.1 ± 0.05	2.4 ± 0.48
Muscle	0.16 ± 0.03	0.15 ± 0.01**	0.15 ± 0.03	0.42 ± 0.06***	0.3 ± 0.06**
Bone	8.2 ± 2.5	4.0 ± 0.34*	3.6 ± 0.49*	9.2 ± 0.7	9.0 ± 1.5
Carcass	0.91 ± 0.15	0.83 ± 0.04	0.53 ± 0.03**	1.4 ± 0.12**	1.3 ± 0.13**

Values are represented as mean ± SD. * $P < 0.05$; ** $P < 0.005$; *** $P < 0.0005$. N/A, not applicable.

antigen-negative C3H mice, confirming the high liver uptake as unspecific hepatic clearance of the radiolabeled Mb (Fig. 5A and Table 1).

For the YTS169 Mb, the radiolabeling, specific activity, and immunoreactive fraction were similar to those of the ^{64}Cu -NOTA-2.43 Mb. The immuno-PET imaging and ex vivo biodistributions in WT B/6 mice using the ^{64}Cu -NOTA-YTS169 Mb were similar to those of ^{64}Cu -NOTA-2.43 Mb in B/6 mice (Fig. 5B and Table 2). Interestingly, the %ID/g in the liver and spleen of the ^{64}Cu -NOTA-YTS169 Mb in C3H mice is reduced by 29% and 48%, respectively, compared with B/6 mice (Fig. 5B and Table 2).

Finally, the ^{64}Cu -NOTA-2.43 Mb was injected into B/6 mice that were blocked with coinjection of 80 μg (4 mg/kg) cold 2.43 Mb or had received anti-CD8 antibody depletion therapy (16 mg/kg for three consecutive days). Immuno-PET images and ex vivo biodistribution acquired 4 h p.i. of antigen-blocked and antigen-depleted mice (Fig. 6B and C and Table 2) showed similar uptake in the spleen ($18 \pm 1.9\%$ ID/g and $15 \pm 1.0\%$ ID/g, respectively) and lymph nodes ($5.0 \pm 1.3\%$ ID/g and $4.5 \pm 2.7\%$ ID/g, respectively) relative to the antigen-negative C3H and NSG mice. CD8 depletion was confirmed using flow cytometry as described above.

Discussion

The two anti-CD8 Mbs developed here for ^{64}Cu immuno-PET imaging of CD8 expression retain their respective antigen specificities following engineering to the Mb format. Both produced

at high yields in mammalian cell culture and could be purified using one-step immobilized metal affinity purification. In vivo studies demonstrated that both Mbs target the spleen and lymph nodes of antigen-positive mice. The lymph node uptake determined from the PET images is lower than the ex vivo biodistribution values due to the partial volume effect encountered when imaging small objects near or below the spatial resolution of the PET scanner (1.5 mm for the Inveon scanner). It has been calculated that a naive lymph node contains $\sim 10^6$ cells (18) and that 7–12% of the leukocytes in the lymph node are CD8^+ . This would suggest that we are able to detect an estimated 70,000–120,000 CD8^+ cells in a mouse lymph node. We have also demonstrated that our engineered antibody fragments lacking the full Fc domain do not deplete CD8^+ T cells in vivo, a critical feature in the development of a biologically inert imaging agent targeting immune cells. Mbs lacking the $\text{C}_\text{H}2$ domain do not have effector functions because they cannot bind $\text{Fc}\gamma$ receptors. However, further studies need to be performed to see if CD8 cross-linking due to the bivalent nature of the Mb activates CD8^+ T cells in vivo.

Due to the low blood activity at only 4 h p.i., immuno-PET images were acquired at relatively early times p.i. compared with other Mb fragments. The 2.43 and YTS169 Mbs have 0.3–0.9% ID/g in the blood of antigen-positive mice when other reports indicate 6–7.5%ID/g at 6 h p.i. (19). The rapid clearance of the anti-CD8 Mbs could be due not only to the reduced size of the Mb compared with the intact antibody, but to the abundance of

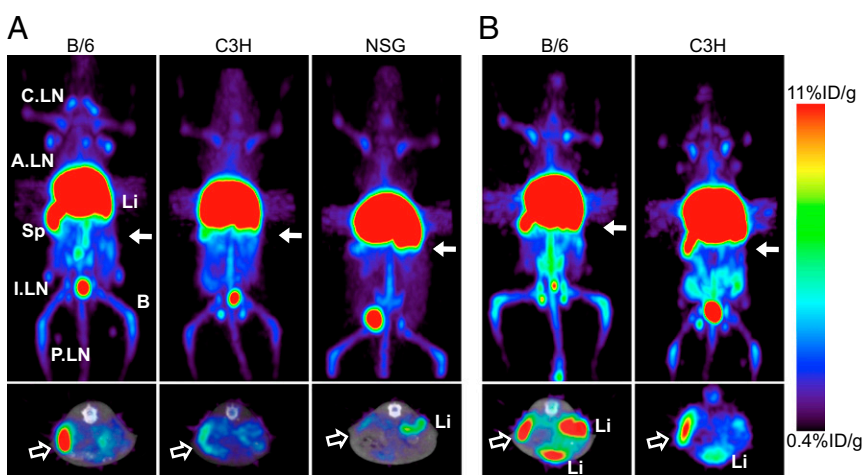


Fig. 5. Immuno-PET imaging of ^{64}Cu -NOTA-2.43 Mb and ^{64}Cu -NOTA-YTS169 Mb shows in vivo specificity of the 2.43 Mb to Lyt2.2^+ mice. (A) ^{64}Cu -NOTA-2.43 Mb was injected into B/6, C3H, and NOD SCID gamma mice for immuno-PET imaging 4 h p.i. (B) ^{64}Cu -NOTA-YTS169 Mb was injected into B/6 and C3H mice for immuno-PET imaging 4 h p.i. Solid white arrows (Upper; 20-mm coronal MIPs) indicate where the transverse images (Lower; 2-mm MIPs) are acquired. Hollow white arrows indicate the location of the spleen.

Table 2. Ex vivo biodistribution analysis of ^{64}Cu -NOTA-YTS169 Mb 4 h p.i. in Lyt2.2⁺ B/6 mice and Lyt2.1⁺ C3H mice

Organ	%ID/g		%ID	
	WT B/6 (n = 3)	WT C3H (n = 3)	WT B/6 (n = 3)	WT C3H (n = 3)
Blood	0.33 ± 0.07	0.25 ± 0.01	N/A	N/A
Axillary lymph nodes	5.1 ± 1.1	5.8 ± 0.66	0.04 ± 0.01	0.09 ± 0.01*
Spleen	49 ± 3.5	26 ± 1.7**	2.7 ± 0.10	2.4 ± 0.06
Stomach	0.76 ± 0.20	0.40 ± 0.15	0.26 ± 0.04	0.17 ± 0.02
Intestines	2.8 ± 0.21	2.3 ± 0.34	3.3 ± 0.44	3.0 ± 0.39
Liver	60.4 ± 1.5	43 ± 2.2**	39 ± 1.0	38 ± 5.0
Kidneys	3.8 ± 0.76	2.6 ± 0.20	0.77 ± 0.21	0.69 ± 0.02
Thymus	0.31 ± 0.03	0.33 ± 0.09	0.01 ± 0.001	0.01 ± 0.002
Heart	0.81 ± 0.02	0.90 ± 0.07	0.07 ± 0.002	0.08 ± 0.01
Lungs	2.1 ± 0.20	1.9 ± 0.11	0.22 ± 0.03	0.26 ± 0.02
Muscle	0.09 ± 0.01	0.06 ± 0.01**	0.01 ± 0.001	0.01 ± 0.001
Bone	7.2 ± 0.81	3.06 ± 0.28*	0.38 ± 0.03	0.23 ± 0.004*
Carcass	0.69 ± 0.05	0.53 ± 0.01*	8.5 ± 0.59	8.8 ± 0.05

Values are represented as mean ± SD. * $P < 0.05$; ** $P < 0.005$. N/A, not applicable.

naturally expressed CD8 antigen throughout the body, termed the antigen sink. This results in rapid accumulation of the radiotracer in organs outside of the blood but makes imaging nonantigen sink organs (i.e., a tumor) difficult. The rapid biological $t_{1/2}$ of these novel Mbs, however, is well matched to the intermediate physical $t_{1/2}$ of ^{64}Cu (12.7 h) immuno-PET radionuclide compared with other positron emitters, including ^{18}F (1.8 h), ^{124}I (100.2 h), and ^{89}Zr (78.4 h).

Recent studies imaging CD20 in a human CD20-expressing transgenic mouse model using ^{64}Cu - or ^{89}Zr -radiolabeled rituximab mimic the targeting ability of the CD8 Mbs in vivo because the abundance and location of CD8 and CD20 antigen expression are similar in vivo (20, 21). Unlike the work presented here, the radiolabeled rituximab is still biologically active and not ideal for imaging studies. Engineering rituximab to other antibody formats could decrease the Fc-dependent biological activity of the imaging radiopharmaceutical (22, 23). In the context of

tumor targeting, this antigen sink has been overcome by blocking endogenous target with cold antibody either during (bolus injection) or before (predosing/blocking injection) administration of the radiotracer. Blocking studies were performed in the human CD20 transgenic model that resulted in an increased radiotracer blood $t_{1/2}$ that could greatly influence the ability to target CD20⁺ B-cell lymphomas in vivo. In fact, the FDA-approved radioimmunotherapeutic Zevalin, a ^{90}Y -radiolabeled anti-CD20 antibody, requires a predose of cold rituximab to block accumulation of the ^{90}Y radioimmunotherapeutic in the spleen and to increase targeting of lymphoma cells (24).

The technique of bolus or predosing injections has proven important for targets other than immunological cell surface molecules where antigen sinks exist. Bolus injections were used recently, for example, in an ^{89}Zr -radiolabeled trastuzumab immuno-PET study that required high doses for reliable targeting in patients due to shed extracellular domain of HER2 in the plasma (25). Also, both ^{111}In -radiolabeled anti-EGF receptor and anti-VEGF receptor antibodies demonstrated high lung and/or liver uptake that could be reduced and tumor uptake enhanced when higher protein doses were injected (26, 27). Furthermore, the concept of blocking the antigen sink has repercussions in the field of therapeutic antibody-drug conjugates. For example, predosing injections were used to block the antigen sink of tomoregulin, or TENB2, a transmembrane protein overexpressed in prostate tumors, to increase the therapeutic index of the monomethyl auristatin E-conjugated anti-TENB2 antibody (28). This study also highlights the fine balance between efficient blocking of the antigen sink vs. displacing the tumor uptake. The ability of these anti-CD8 Mb fragments to image either CD8⁺ lymphomas or tumor-infiltrating CD8⁺ T cells, for example, might rely on efficiently blocking the antigen sink for consistent targeting.

The rapid clearance of the anti-CD8 Mbs could also be due to the presence of multimers, causing increased liver uptake at early time points. At 4 h p.i., the CD8 Mbs have ~60–70%ID/g in the liver, compared with other ^{64}Cu -radiolabeled Mbs that range from 15 to 32.4%ID/g at 4–5 h p.i. (19, 29). Nonspecific liver uptake and retention occur when using ^{64}Cu due to the transchelation of copper to enzymes in the liver (30). However, an Mb dimer (~160 kDa) is similar in size to an intact antibody but lacks the full Fc domain that allows for neonatal Fc receptor recycling. When injected with ^{64}Cu -NOTA-YTS169 Mb, both B/6 and C3H mice showed decreased uptake in lymph nodes, spleen, and blood compared with the ^{64}Cu -NOTA-2.43 Mb. This could be attributed to the higher amount of multimer in the YTS169 Mb than in the 2.43 Mb, as shown by SEC, accelerating hepatic clearance and resulting in a decreased blood $t_{1/2}$ and lower ability to target lymph nodes. It

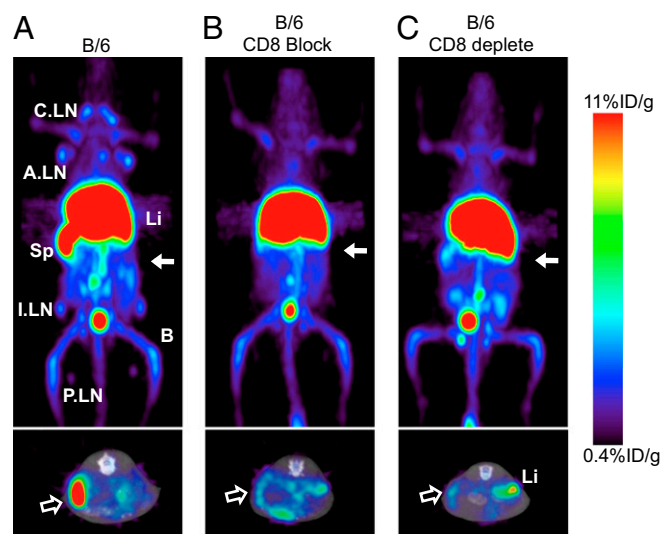


Fig. 6. Immuno-PET imaging of ^{64}Cu -NOTA-2.43 Mb in antigen-blocked and antigen-depleted B/6 mice is shown. Immuno-PET images were acquired 4 h p.i. of ^{64}Cu -NOTA-2.43 Mb into: WT B/6 (A), B/6 mice blocked with 4 mg/kg of cold Mb (B), and B/6 mice treated with an anti-CD8-depleting antibody (C). Solid white arrows (Upper, 20-mm coronal MIPs) indicate where the transverse images (Lower, 2-mm MIPs) are acquired. (Lower) Hollow white arrows indicate the location of the spleen.

should be noted that the Mb multimers of both YTS169 and 2.43 importantly retain their ability to bind sCD8 α β , as shown by SEC. Potential aggregation/dimerization due to inter-V_H-V_L binding can be reduced, for example, by engineering two cysteines that stabilize the interaction between V_H and V_L, among other methods (31, 32).

The ⁶⁴Cu-NOTA-YTS169 Mb that binds both Lyt2.1 and Lyt2.2 expressed in different mouse strains showed varying uptake in the spleens and livers of B/6 and C3H mice. In this study, however, the C3H mice were 20 wk old and the B/6 mice were 8 wk old, with average spleen and liver weights of either 96 \pm 9 mg and 883 \pm 43 mg or 54 \pm 3 mg and 653 \pm 10 mg, respectively. Therefore, the weights of the organs greatly affect the %ID/g, and the actual %ID per organ 4 h p.i. is similar in the spleen and liver (Table 2). This highlights an important fact that %ID/g values are not consistent for every experiment but are very reproducible within groups of mice of the same age and weight.

The development of these anti-CD8 immuno-PET radiotracers will be beneficial for studying a host of preclinical disease models, including, but not limited to, lymphoma detection and tumor T-cell infiltration. Preclinical immunotherapy models enhancing the dynamic function and proliferation of cytotoxic T cells could potentially be monitored noninvasively in vivo using immuno-PET. Furthermore, the lessons learned in a preclinical setting will prove beneficial for the development and translation of anti-human CD8 antibody fragments for immuno-PET imaging in the clinic.

Conclusion

Described here is the successful development of functional CD8 imaging agents based on engineered antibodies for immuno-PET

imaging in a variety of preclinical disease and immunotherapeutic models. Two allele-specific Mb fragments were produced, characterized, radiolabeled with ⁶⁴Cu, and used in micro-PET imaging to quantify uptake in lymphoid organs in WT mice in vivo. Examining antibody-based immuno-PET imaging of mouse CD8 expression is useful not only for immuno-PET imaging of preclinical models of CD8-based immunotherapy, but it has further implications for the development of an anti-human CD8 antibody or fragment-based immuno-PET imaging agent that is translatable to the clinic.

Materials and Methods

Animal studies were approved by the University of California, Los Angeles (UCLA) Chancellor's Animal Research Committee. Mice were purchased from Jackson Laboratory. Detailed information on animals, cloning, Mb and recombinant antigen design, protein expression and purification, protein conjugation, flow cytometry, depletion assays, radiolabeling, immuno-PET imaging, biodistribution, and data analysis can be found in *SI Materials and Methods*.

ACKNOWLEDGMENTS. We are grateful to Waldemar Ladno, Darin Williams, and Dr. David Stout at the Crump Institute for Molecular Imaging at UCLA for their help with the small-animal PET scans. We thank Drs. Antoni Ribas and Caius Radu for their inspiring discussions. We thank Washington University School of Medicine for the ⁶⁴Cu production. Furthermore, we thank the Jonsson Comprehensive Cancer Center (NIH Grant CA016042), the Genoseq Core Facility, and the Flow Cytometry Core Facility at UCLA. This work was supported by the UCLA Scholars in Oncologic Molecular Imaging training program [National Institutes of Health (NIH) Grant R25T CA098010] and by the California Institute for Regenerative Medicine (Grant RT1-01126-1). M.N.M. is supported by California Institute for Regenerative Medicine Training Grant TG2-01169. O.N.W. is an investigator of the Howard Hughes Medical Institute.

- Pillay V, Gan HK, Scott AM (2011) Antibodies in oncology. *New Biotechnol* 28(5):518–529.
- Rothe A, Rubbert A (2011) Recombinant proteins in rheumatology—Recent advances. *New Biotechnol* 28(5):502–510.
- Wu AM, Senter PD (2005) Arming antibodies: Prospects and challenges for immunoconjugates. *Nat Biotechnol* 23(9):1137–1146.
- Knowles SM, Wu AM (2012) Advances in immuno-positron emission tomography: Antibodies for molecular imaging in oncology. *J Clin Oncol* 30(31):3884–3892.
- Matsui K, Wang Z, McCarthy TJ, Allen PM, Reichert DE (2004) Quantitation and visualization of tumor-specific T cells in the secondary lymphoid organs during and after tumor elimination by PET. *Nucl Med Biol* 31(8):1021–1031.
- Pittet MJ, et al. (2007) In vivo imaging of T cell delivery to tumors after adoptive transfer therapy. *Proc Natl Acad Sci USA* 104(30):12457–12461.
- Nair-Gill ED, Shu CJ, Radu CG, Witte ON (2008) Non-invasive imaging of adaptive immunity using positron emission tomography. *Immunol Rev* 221:214–228.
- Yaghoubi SS, Campbell DO, Radu CG, Czernin J (2012) Positron emission tomography reporter genes and reporter probes: Gene and cell therapy applications. *Theranostics* 2(4):374–391.
- Koya RC, et al. (2010) Kinetic phases of distribution and tumor targeting by T cell receptor engineered lymphocytes inducing robust antitumor responses. *Proc Natl Acad Sci USA* 107(32):14286–14291.
- Laing RE, Nair-Gill E, Witte ON, Radu CG (2010) Visualizing cancer and immune cell function with metabolic positron emission tomography. *Curr Opin Genet Dev* 20(1):100–105.
- Juweid ME, Cheson BD (2006) Positron-emission tomography and assessment of cancer therapy. *N Engl J Med* 354(5):496–507.
- Mamede M, et al. (2003) Differential uptake of (18)F-fluorodeoxyglucose by experimental tumors xenografted into immunocompetent and immunodeficient mice and the effect of immunomodification. *Neoplasia* 5(2):179–183.
- Ribas A, et al. (2010) Imaging of CTLA4 blockade-induced cell replication with (18)F-FLT PET in patients with advanced melanoma treated with tremelimumab. *J Nucl Med* 51(3):340–346.
- Aarntzen EH, et al. (2011) Early identification of antigen-specific immune responses in vivo by [¹⁸F]-labeled 3'-fluoro-3'-deoxy-thymidine ([¹⁸F]FLT) PET imaging. *Proc Natl Acad Sci USA* 108(45):18396–18399.
- Nair-Gill E, et al. (2010) PET probes for distinct metabolic pathways have different cell specificities during immune responses in mice. *J Clin Invest* 120(6):2005–2015.
- Olafsen T, Wu AM (2010) Antibody vectors for imaging. *Semin Nucl Med* 40(3):167–181.
- Malviya G, Galli F, Sonni I, Pacilio M, Signore A (2010) Targeting T and B lymphocytes with radiolabelled antibodies for diagnostic and therapeutic applications. *Q J Nucl Med Mol Imaging* 54(6):654–676.
- Martin-Fonchea A, et al. (2003) Regulation of dendritic cell migration to the draining lymph node: Impact on T lymphocyte traffic and priming. *J Exp Med* 198(4):615–621.
- Olafsen T, et al. (2005) Optimizing radiolabeled engineered anti-p185HER2 antibody fragments for in vivo imaging. *Cancer Res* 65(13):5907–5916.
- Natarajan A, et al. (2012) Positron emission tomography of ⁶⁴Cu-DOTA-Rituximab in a transgenic mouse model expressing human CD20 for clinical translation to image NHL. *Mol Imaging Biol* 14(5):608–616.
- Natarajan A, Habte F, Gambhir SS (2012) Development of a Novel Long-Lived ImmunoPET Tracer for Monitoring Lymphoma Therapy in a Humanized Transgenic Mouse Model. *Bioconjug Chem* 23(6):1221–1229.
- Olafsen T, et al. (2010) ImmunoPET imaging of B-cell lymphoma using ¹²⁴I-anti-CD20 scFv dimers (diabodies). *Protein Eng Des Sel* 23(4):243–249.
- Olafsen T, et al. (2009) Recombinant anti-CD20 antibody fragments for small-animal PET imaging of B-cell lymphomas. *J Nucl Med* 50(9):1500–1508.
- Witzig TE, et al. (1999) Phase III trial of IDEC-Y2B8 radioimmunotherapy for treatment of relapsed or refractory CD20(+) B-cell non-Hodgkin's lymphoma. *J Clin Oncol* 17(12):3793–3803.
- Dijkers EC, et al. (2010) Biodistribution of ⁸⁹Zr-trastuzumab and PET imaging of HER2-positive lesions in patients with metastatic breast cancer. *Clin Pharmacol Ther* 87(5):586–592.
- Bumbaca D, et al. (2012) Maximizing tumour exposure to anti-neuropilin-1 antibody requires saturation of non-tumour tissue antigenic sinks in mice. *Br J Pharmacol* 166(1):368–377.
- Divgi CR, et al. (1991) Phase I and imaging trial of indium 111-labeled anti-epidermal growth factor receptor monoclonal antibody 225 in patients with squamous cell lung carcinoma. *J Natl Cancer Inst* 83(2):97–104.
- Boswell CA, et al. (2012) Differential effects of pre dosing on tumor and tissue uptake of an ¹¹¹In-labeled anti-TENB2 antibody-drug conjugate. *J Nucl Med* 53(9):1454–1461.
- Wu AM, et al. (2000) High-resolution microPET imaging of carcinoembryonic antigen-positive xenografts by using a copper-64-labeled engineered antibody fragment. *Proc Natl Acad Sci USA* 97(15):8495–8500.
- Rogers BE, et al. (1996) Comparison of four bifunctional chelates for radiolabeling monoclonal antibodies with copper radioisotopes: Biodistribution and metabolism. *Bioconjug Chem* 7(4):511–522.
- Glockshuber R, Malia M, Pfützinger I, Plückthun A (1990) A comparison of strategies to stabilize immunoglobulin Fv-fragments. *Biochemistry* 29(6):1362–1367.
- Wörn A, Plückthun A (2001) Stability engineering of antibody single-chain Fv fragments. *J Mol Biol* 305(5):989–1010.